



New constraint on land carbon cycle

Deliverable 1.7

Authors: Philippe Peylin, Philippe Ciais, Ryan Padron Flasher, Sonia Seneviratne, Laibao Liu



This project received funding from the Horizon 2020 programme under the grant agreement No. 821003.

Document Information

GRANT AGREEMENT	821003
PROJECT TITLE	Climate Carbon Interactions in the Current Century
PROJECT ACRONYM	4C
PROJECT START DATE	1/6/2019
RELATED WORK PACKAGE	WP1
RELATED TASK(S)	T1.1
LEAD ORGANIZATION	CEA-LSCE
AUTHORS	Philippe Peylin, Philippe Ciais, Ryan Padron Flasher, Sonia Seneviratne, Laibao Liu
SUBMISSION DATE	26/02/20121
DISSEMINATION LEVEL	PU

History

DATE	SUBMITTED BY	REVIEWED BY	VISION (NOTES)
24/02/2021	Philippe Peylin (CEA-LSCE)		
26/02/2021		Stephen Sitch, Pierre Friedlingstein (UNEXE)	

Please cite this report as: P. Peylin, P. Ciais, R. Padron Flasher, S. Seneviratne, L. Liu (2021), New constraints on land carbon, D1.7 of the 4C project

Disclaimer: The content of this deliverable reflects only the author's view. The European Commission is not responsible for any use that may be made of the information it contains.

Table of Contents

1	Introduction	6
2	New constraints on the land net carbon fluxes	6
2.1	Machine learning based forest net CO ₂ flux data	6
3	New constraints on the land gross carbon fluxes	12
3.1	Atmospheric COS constraint on gross primary production.....	12
3.2	Solar-induced fluorescence constraint on gross primary production.....	15
3.3	Observation-based water fluxes to constrain land carbon fluxes	18
4	Publications from this deliverable	20
5	Additional references	20

List of tables

Table 1: Net Ecosystem Productivity (NEP) up-scaled from EC networks with a global age-NEP relationship (AC), and with biome-specific age-NEP relationships (BAC). The net carbon balance (NBP) is derived from NEP by adding C losses not monitored by flux towers. Independent NBP from measured biomass carbon stock changes and modeled soil carbon change is from the global synthesis of Pan et al.	8
--	---

List of figures

Figure 1: Forest age distribution for four biomes derived from the forest age map used to upscale NEP. In red is the sampling of forests age by flux towers.	9
---	---

Figure 2: Biome-specific NEP-age relationships from chronosequence sites (in blue) used in the BAC approach, compared with the global NEP-age relationship deduced from the FLUXNET network (in red) used in the AC model.	10
Figure 3: Spatial distribution of NEP derived from three approaches. (a) BAC: NEP up-scaled from EC with biome NEP-age curves, age maps, environmental variables; (b) AC: NEP up-scaled directly from EC data, age-maps and environmental variables; (c) C: NEP up-scaled from EC data without age information....	11
Figure 4: Flowchart of the procedure used for the calculation of COS and CO ₂ concentrations from land surface model outputs. Different sources and sinks of COS (COS flux scenario) and CO ₂ (CO ₂ flux scenario) are calculated from flux maps and/or empirical modeling and transported to cover the globe using the French transport model LMDZ.	13
Figure 5: Temporal evolution of the COS concentration at Point Barrow station (Alaska) (left) and temporal evolution of the seasonal amplitude of the seasonal cycle at all stations of the NOAA network (see location in the previous figure). The observations are taken from the NOAA/ESRL global monitoring network....	14
Figure 6: Distributions of the LRU values computed from the mechanistic approach, using a monthly climatology of simulated COS and GPP fluxes over the 2000-2009 period. Each subplot represents one of the 14 PFTs used in ORCHIDEE. The x-axis represents the LRU value and the y-axis the occurrences. The red vertical bar represents the median LRU value, the green one the LRU optimal value that minimizes the difference between the mechanistic and the LRU approaches.	15
Figure 7: Examples of temporal variations of the SIF products for two clusters of each plant functional type (year 2015). The lines correspond to the means of the corresponding cluster and the dots to the actual products, with a different colour for each product. For OCO-2, the time series are shown for the raw (@757 nm) and spectrally scaled (@740 nm) data. The number of pixels considered in each cluster is indicated. The PFTs are tropical evergreen broadleaf (TrEBF), tropical deciduous broadleaf (TrDBF), temperate evergreen needleleaf (TeENF), temperate evergreen broadleaf (TeEBF), temperate deciduous broadleaf (TeDBF), boreal evergreen needleleaf (BorENF), boreal deciduous broadleaf (BorDBF), boreal deciduous needleleaf (BorDNF), forests, C3 grasslands (temperate—TeC3GRA, tropical— TroC3GRA, and boreal— BorC3GRA) and C4 grasslands (C4GRA), and C3 (C3CRO) and C4 (C4CRO) crops.....	17
Figure 8: Change in dry season water availability from the recent period 1985–2014 relative to the period 1902–1950 based on the reconstructions from (a) data-driven models (DDM) and (b) land surface models (LSM).	19
Figure 9: Atmospheric data sets contributing to the ensemble reconstruction of global runoff (Ghiggi et al, in review).	19

About 4C

Climate-Carbon Interactions in the Coming Century (4C) is an EU-funded H2020 project that addresses the crucial knowledge gap in the climate sensitivity to carbon dioxide emissions, by reducing the uncertainty in our quantitative understanding of carbon-climate interactions and feedbacks. This will be achieved through innovative integration of models and observations, providing new constraints on modelled carbon-climate interactions and climate projections, and supporting Intergovernmental Panel on Climate Change (IPCC) assessments and policy objectives.

Executive Summary

This deliverable describes four data-based products on both the net land ecosystem CO₂ exchange and the vegetation gross CO₂ exchange, namely the Gross Primary Productivity (GPP). The first constraint concerns forest ecosystems with the estimation of the spatial distribution of net ecosystem productivity (NEP). Two different machine learning approaches are used to extrapolate in-situ NEP measurements using specific predictors such as forest age distribution, biome-specific age – NEP relationships and climate. The first constraint on gross primary productivity is provided by atmospheric COS measurements with a specific modeling framework to evaluate large scale dynamics of GPP. It is based on an atmospheric transport model that relates GPP-derived COS fluxes to atmospheric COS. The second constraint arise from solar-induced chlorophyll fluorescence (SIF) derived from satellite measurements. SIF measurements is directly related to photosynthesis activity, providing information on spatial and temporal variations of GPP (especially the responses to drought). Finally, estimates of the dynamics of terrestrial water balance is used to provide new constraint on the land carbon cycle, mainly through water availability to plants.

The different products highlight the advances made within the 4C project to provide new constraints on the land carbon cycle based on recent in situ and satellite measurements combined with novel techniques. All data products presented in this deliverable report are freely accessible (see respective “data availability” section) and serve as novel constraints for the partner work packages within the 4C project.

Keywords

Land carbon, GPP, COS, Solar-Induced fluorescence, forest carbon, soil moisture

1 Introduction

The objective of this report is to describe new observational constraints on the global and regional land CO₂ fluxes to support quantitative understanding of the carbon cycle. This new set of constraints, together with complementary global and regional ocean constraints (described in a separate deliverable) will provide independent information on the partitioning of land and ocean fluxes and help determine the origins and causes of the carbon budget imbalance. The new constraints are grouped into two sets:

- The first one concerns the net forest carbon fluxes.
- The second set concerns the gross land carbon fluxes, with constraint on the gross primary production (GPP) derived from atmospheric measurements of carbonyl sulfide (COS), solar-induced fluorescence and soil moisture dynamics.

2 New constraints on the land net carbon fluxes

2.1 Machine learning based forest net CO₂ flux data

Most of the global land carbon (C) sink is in forest biomes but current observations do not provide an accurate spatial distribution. On the one hand, biomass inventories have a good coverage of managed forests, but they are very sparse both in tropical and unmanaged forests. In addition, inventories measure biomass stock changes from repeated sampling campaigns, but changes in soil C are modeled, not observed. On the other hand, global maps of C dioxide (CO₂) fluxes obtained from top-down atmospheric inversions have a too coarse spatial resolution for accurately separating forests from other biomes and such technique is very sensitive to transport model errors. Eddy covariance (EC) networks form a global observing system measuring local net CO₂ fluxes across various ecosystems with more than 200 flux towers in forest ecosystems. Net ecosystem productivity (NEP) from flux towers can be separated into gross CO₂ uptake by photosynthesis (GPP) and losses from ecosystem respiration (ER). Machine learning (ML) algorithms have paved the way to characterize the spatiotemporal variations of GPP and surface energy fluxes related to climate drivers despite the uneven coverage of the network. However, a realistic global spatial distribution of NEP from flux towers has never been obtained. For instance, the global mean NEP up-scaled from flux towers for all land ecosystems, was an implausibly large sink of $\approx 18 \text{ Pg C a}^{-1}$. So far, forest inventories are used for carbon changes in tree biomass, and atmospheric inversions for estimating the net CO₂ fluxes of large regions. But global EC measurements have failed to provide independent estimates of the global carbon balance of ecosystems, largely due to

challenges in correctly up-scaling fluxes from local to global scales. As a consequence, the gap between site-scale EC observation and global patterns of forests C fluxes has not been closed.

We developed two ML methods to estimate the spatial distribution of forest NEP over the globe by accounting for age and climate. The first approach called BAC (Biome, Age, Climate) combines biome-specific NEP-age curves obtained from a compilation from forest site data (known as chronosequences), a new gridded map of forest age retrieved from forest census data and remote sensing, gridded annual temperature (MAT), growing-season length and gridded GPP up-scaled from flux towers (the FLUXCOM products using remote sensing data strictly limited to forests in order to minimize the mixed effects from other vegetation types). The training of the BAC algorithm is performed with local NEP, GPP measurements and local forest age from a harmonized FLUXNET dataset of more than 120 flux towers.

The second approach called AC (Age, Climate) is based on the empirical model proposed by Jung et al. where NEP is regressed from local flux tower observations using site-age, climate and GPP, then up-scaled using the same forest age maps, MAT and GPP fields than in BAC method. The key difference between the two algorithms is that AC makes use of a single global NEP-age relationship deduced directly from the FLUXNET data despite their uneven age sampling, whereas BAC takes additional a priori information from the biome-specific NEP-age chronosequences. Note that wet tropical sites NEP data were corrected for low nighttime turbulence, based on original publications. The annual NEP maps were produced at 0.5° resolution and represent the period of the last decade.

We show in Figure 1 the distribution of forest age, and in Figure 2 the biome-specific NEP-age relationships used in the BAC method, and the global relationship used in the AC one. The area occupied by very young forests in Figure 1a reflects recent stand-replacing disturbances, for instance fires in the boreal region (Figure 2). The biome-specific NEP-age curves used in the BAC approach shown in Figure 3 have a common shape characteristic of the carbon balance of forests recovering from disturbance. NEP of recently disturbed forests is a net source of CO₂ to the atmosphere dominated by the decomposition of soil carbon and woody debris as a legacy from earlier disturbance. NEP of young forests that accumulate biomass is a strong CO₂ sink peaking between 40 and 60 years, depending on biome. NEP of old forests tends to smaller CO₂ sources or sinks in the set of chronosequences compiled here. Generally, the time after disturbance at which NEP goes from source to sink is longer in the tropics (≈40 years) than in boreal and temperate regions (≈ 10 to 20 years) as observed in Figure 3. A similar behaviour was observed for instance at the Tapajos forest in southern Amazonia: the site was still a source 30 years after a disturbance from decaying dead trees, despite the fact that live trees accumulated biomass at high rates.

The two ML approaches to upscale NEP give large carbon sinks in tropical and temperate forests, while the boreal forest biome is only a small sink (Table 1). Larger NEP sinks prevail in the young and productive temperate forests of Western Europe and the Eastern US, and in temperate and subtropical forests of China. In China, recent plantations drive young ages and high NEP uptake (Figure b). Boreal forests take up CO₂ in North America, but they are small sources in Northern Siberia (Figure). In the tropics, both ML up-scaling methods point out to wet forests being smaller sinks per unit area than dry forests and woodlands (Figure) despite the wet forests being much more productive. Despite similarities in geographic patterns of NEP, regional NEP budgets are rather close between the AC and the BAC up-scaling approaches (Table 1). Compared with previous estimates of tropical forest NEP based on flux towers being a sink of 8 Pg C a⁻¹, the data in Table 1 give a smaller NEP. This is not because age is explicitly accounted for in this study, but because sites with low nighttime turbulence were removed (see comparison of BAC and AC with up-scaling using only climate and GPP in SI). Interestingly, the mean NEP of dry tropical forests is similar to the one of wet tropical forests (Table 1) despite GPP of dry forests being lower. Such a large NEP in dry tropical forests and woodlands in our approach comes from the fact that most of the FLUXNET towers in dry regions are locally large CO₂ sinks with suppressed respiration. Nonetheless, those towers are mainly from Mediterranean forests, which may not be good analogues of dry tropical forests. At face value, dry tropical forests have been observed to accumulate carbon at rather high rates between two fire disturbance events.

Table 1: Net Ecosystem Productivity (NEP) up-scaled from EC networks with a global age-NEP relationship (AC), and with biome-specific age-NEP relationships (BAC). The net carbon balance (NBP) is derived from NEP by adding C losses not monitored by flux towers. Independent NBP from measured biomass carbon stock changes and modeled soil carbon change is from the global synthesis of Pan et al.

	Net Ecosystem Productivity NEP		Net Carbon Balance NBP		NBP from biomass inventories
	AC	BAC	AC	BAC	Pan <i>et al.</i>
Boreal	0.7	0.5	0.3 ± 0.2	0.1 ± 0.2	0.5 ± 0.1
Temperate	2.1	2.1	1.7 ± 0.2	1.7 ± 0.2	0.8 ± 0.1

Tropics	3.1	3.6	1.8 ± 0.5	1.8 ± 0.5	2.8 ± 0.7
<i>Wet tropics</i>	<i>1.6</i>	<i>2.1</i>	<i>0.8 ± 0.3</i>	<i>1.0 ± 0.3</i>	<i>N/A</i>
<i>Dry tropics</i>	<i>1.6</i>	<i>1.5</i>	<i>1.0 ± 0.2</i>	<i>0.9 ± 0.2</i>	<i>N/A</i>
Globe	6.6 ± 0.7	6.5 ± 0.7	4.0 ± 0.9	3.9 ± 0.8	4.1 ± 0.7

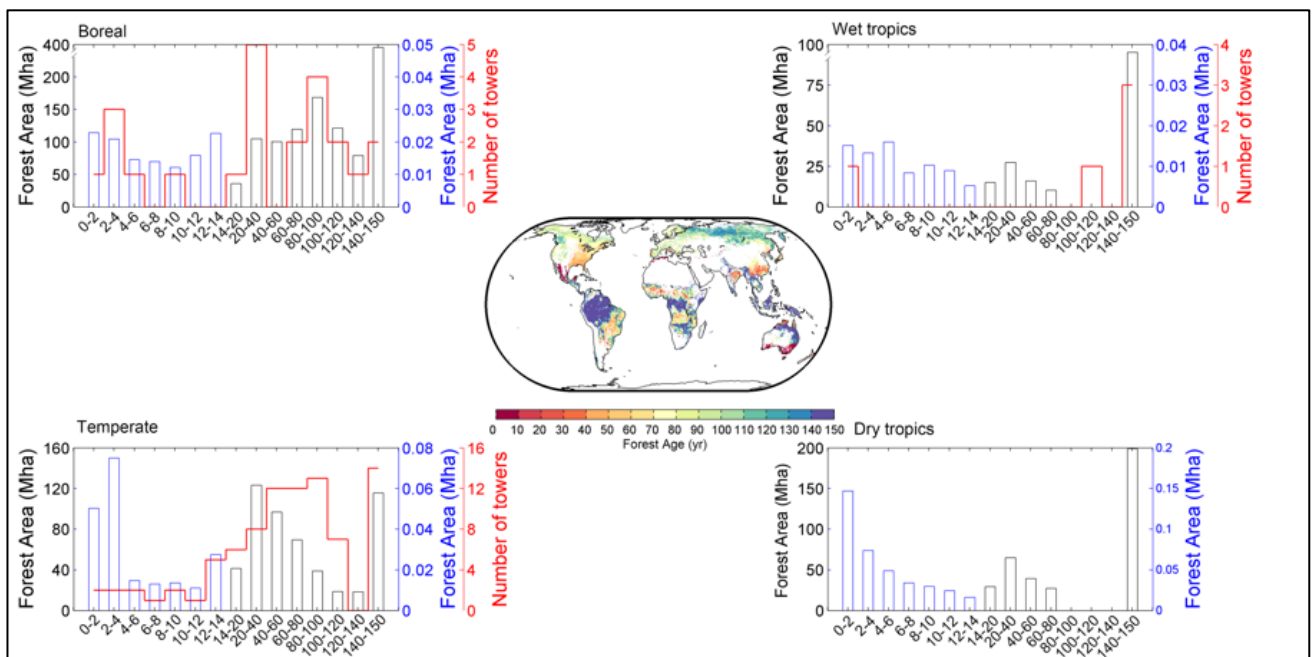


Figure 1: Forest age distribution for four biomes derived from the forest age map used to upscale NEP. In red is the sampling of forests age by flux towers.

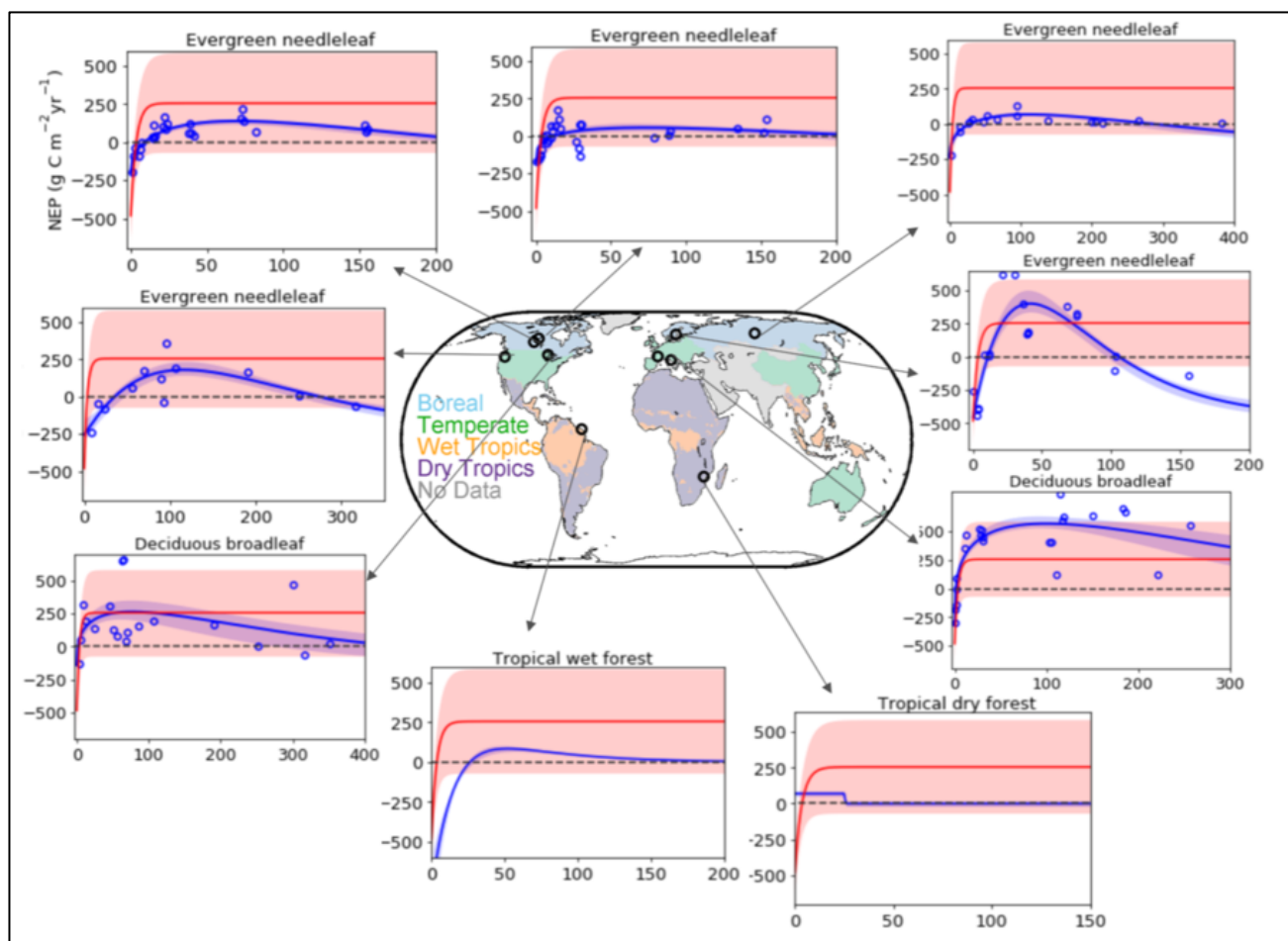
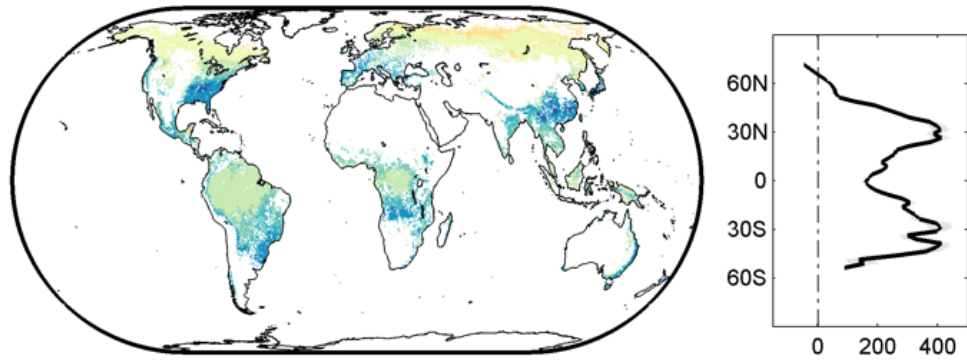
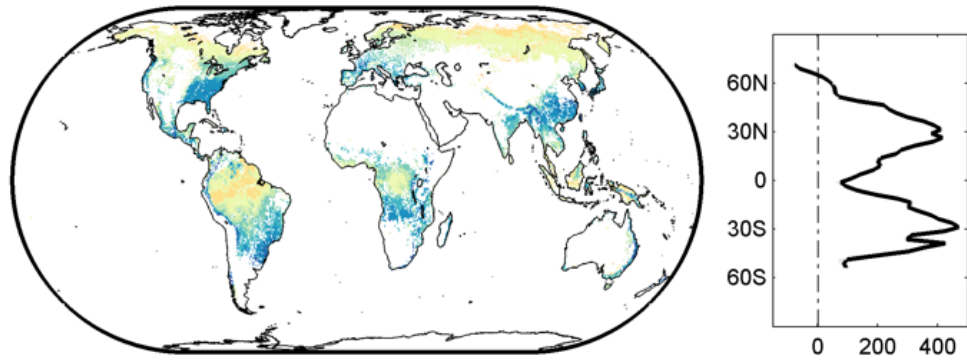


Figure 2: Biome-specific NEP-age relationships from chronosequence sites (in blue) used in the BAC approach, compared with the global NEP-age relationship deduced from the FLUXNET network (in red) used in the AC model.

(a) BAC



(b) AC



(c) C

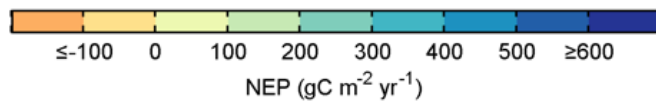
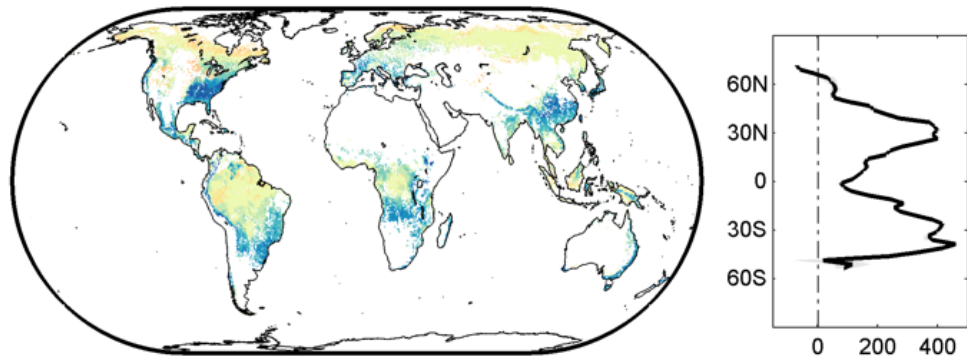


Figure 3: Spatial distribution of NEP derived from three approaches. (a) BAC: NEP up-scaled from EC with biome NEP-age curves, age maps, environmental variables; (b) AC: NEP up-scaled directly from EC data, age-maps and environmental variables; (c) C: NEP up-scaled from EC data without age information.

3 New constraints on the land gross carbon fluxes

3.1 Atmospheric COS constraint on gross primary production

Carbonyl sulphide (COS) has been recognized to be a promising surrogate of CO₂ for tracking the amount of carbon that is absorbed by the terrestrial vegetation (see recent synthesis by Whealan et al. 2018). Indeed, COS follows the same diffusion pathway into the leaf chloroplasts. While absorbed CO₂ following photosynthesis is re-emitted to the atmosphere through respiration processes, COS is nearly fully consumed by the enzyme carbonic anhydrase within the leaves. Therefore, the atmospheric drawdown of COS reflects to a large extent the plant uptake of COS, provided that the non-leaf COS fluxes have a much smaller temporal variability. In this respect, COS acts as a tracer of the CO₂ assimilation by plants (gross primary production, GPP). Launois et al. (2015) using atmospheric measurements of CO₂ and COS and a simple assimilation scheme of COS by terrestrial ecosystems have shown the potential of such approach. Recently, Hilton et al. (2017) additionally showed that the variability of the COS temporal gradient is mainly driven by variation in GPP rather than other modelled COS flux.

In this report, we thus propose a new framework to evaluate the Gross Primary Production (GPP) of the land surface models at large scale using the recent measurements of atmospheric COS combined with CO₂ observations. The atmospheric COS and CO₂ concentrations are taken from the National Oceanic and Atmospheric Administration Earth System Research Laboratory (NOAA/ESRL) on the website: <ftp://ftp.cmdl.noaa.gov/> (Montzka et al., 2004).

Figure 4 below details the overall framework and the different COS components. These include absorption by plants and oxic soils, emissions by oceans (both direct and indirect), emissions by anoxic soils and wetlands, anthropogenic sources, emissions by fires and destruction by OH radical in the atmosphere. For the plant related COS uptake, we can use the linear formulation of the COS uptake by leaves as a function of GPP (Sandoval-Soto et al. 2005):

$$F_{\text{COS}} = F_{\text{CO}_2} \times [\text{COS}] / [\text{CO}_2] \times V_{\text{COS}} / V_{\text{CO}_2}$$

where,

F_{COS} and F_{CO_2} are the COS and CO₂ uptake respectively, $[\text{COS}]$ and $[\text{CO}_2]$ being the ambient air concentrations of COS and CO₂ and V_{COS} and V_{CO_2} are the COS and CO₂ leaf uptake velocities. The ratio of uptake velocities, $\text{LRU} = V_{\text{COS}} / V_{\text{CO}_2}$ constitutes the main critical parameter. The LRUs vary by plant functional type (PFTs) and mainly depend on leaf stomatal conductance and light (Seibt et al. 2010). Once the different leaf COS uptake is calculated (from each model GPP) we further use a transport model (LMDZ in this example) to map the fluxes into the atmospheric concentrations (using all components of COS).

The equivalent CO_2 concentration are obtained from the net ecosystem exchange from the same model simulations with the additional contribution of air-sea fluxes (taken from a climatology; Takahashi et al. 2009) and anthropogenic emissions (taken from the Global Carbon Project).

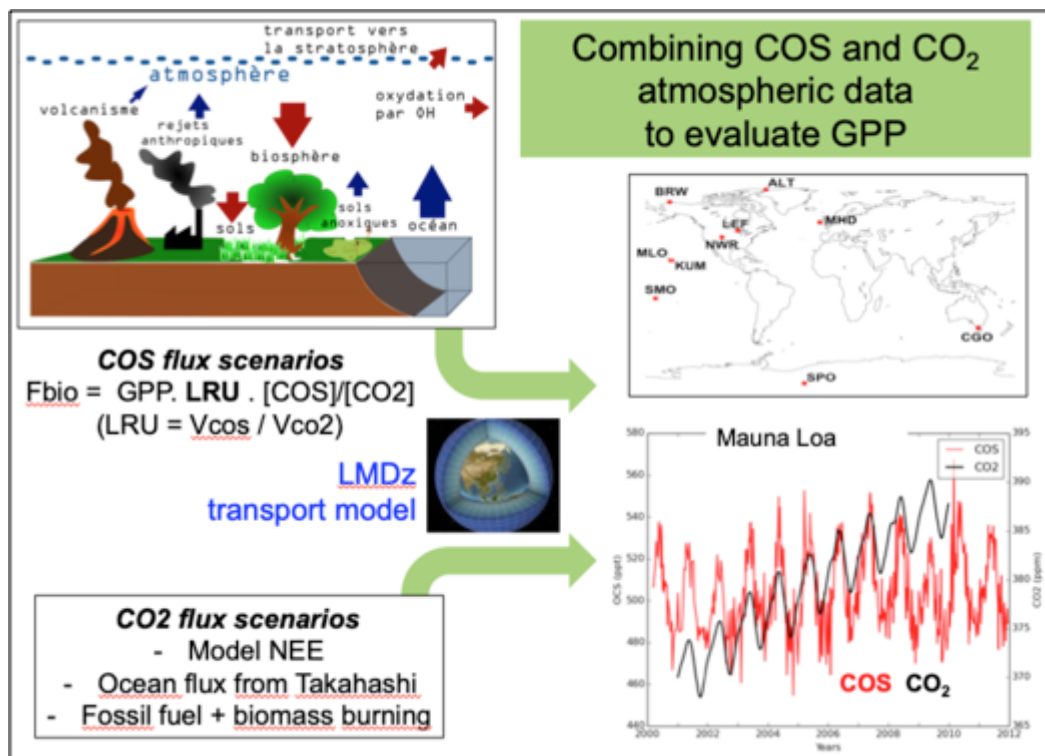


Figure 4: Flowchart of the procedure used for the calculation of COS and CO_2 concentrations from land surface model outputs. Different sources and sinks of COS (COS flux scenario) and CO_2 (CO_2 flux scenario) are calculated from flux maps and/or empirical modeling and transported to cover the globe using the LMDz transport model.

In order to refine/improve the overall methodology we have worked on two aspects:

1/ First we investigated more precisely the potential information content, in terms of seasonal cycle (amplitude and phase) of the atmospheric COS data. Figure 5 displays the temporal evolution of the COS concentrations at the Alert site (left) and the yearly evolution of the amplitude of the COS seasonal cycle at all NOAA stations (right). This figure illustrates the variation of the COS from year to year, with for instance a smaller amplitude of the COS at ALT for 2014 compared to the preceding/following years. These year-to-year variations are likely to be primarily the response of year-to-year variations in the GPP fluxes.

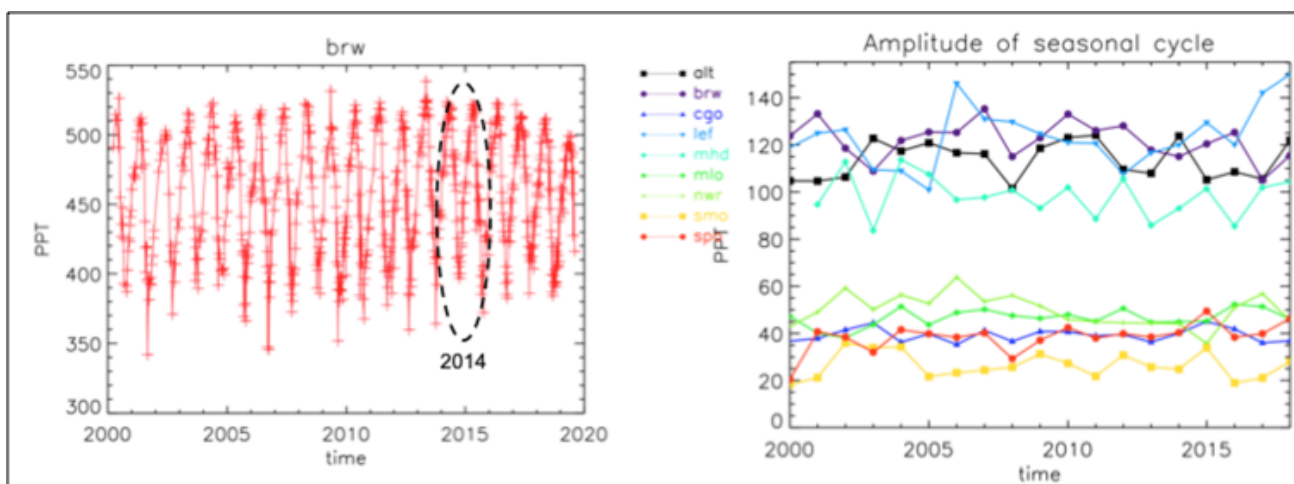


Figure 5: Temporal evolution of the COS concentration at Point Barrow station (Alaska) (left) and temporal evolution of the seasonal amplitude of the seasonal cycle at all stations of the NOAA network (see location in the figure 4). The observations are taken from the NOAA/ESRL global monitoring network.

2/ The Leaf Relative Uptake (LRU) of COS is a critical parameter in this approach. We have thus used a mechanistic approach to calculate with the ORCHIDEE land surface model the LRU for all ecosystems. Such work led us to define spatio-temporal variations of LRU to be used with the GPP of each land surface model (see Figure 4 for the approach). This work is under publication in Biogeosciences (Maignan et al., in review) and the figure 6 below illustrates the main results with respect to the optimal LRU values for the different PFTs of the ORCHIDEE model.

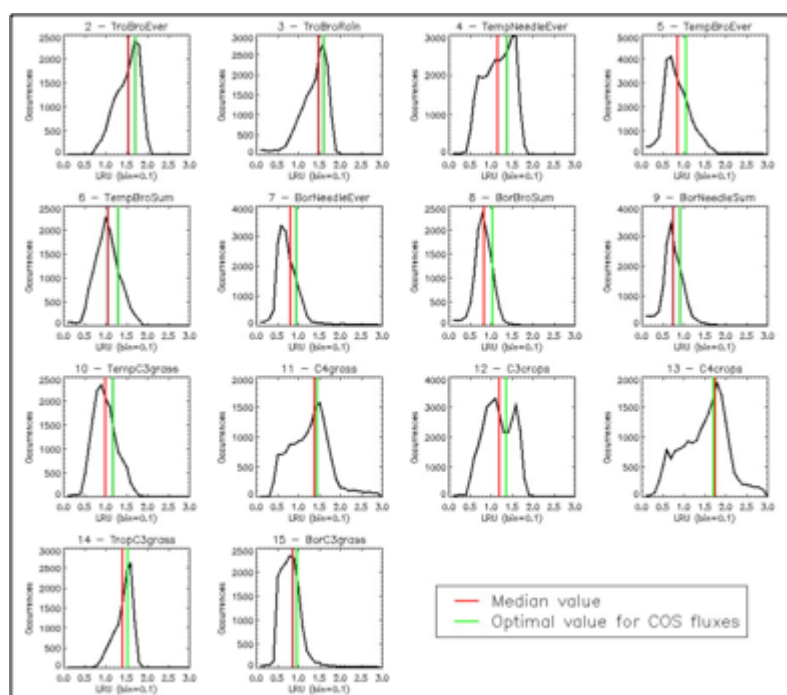


Figure 6: Distributions of the LRU values computed from the mechanistic approach, using a monthly climatology of simulated COS and GPP fluxes over the 2000-2009 period. Each subplot represents one of the 14 PFTs used in ORCHIDEE. The x-axis represents the LRU value and the y-axis the occurrences. The red vertical bar represents the median LRU value, the green one the LRU optimal value that minimizes the difference between the mechanistic and the LRU approaches.

3.2 Solar-induced fluorescence constraint on gross primary production

Since the first evidenced linear relationship between remotely-sensed solar-induced chlorophyll fluorescence (SIF) and GPP at broad spatial and temporal scales (Guanter et al., 2014; Zhang et al., 2016), it is anticipated that satellite SIF products will provide a significant constraint (reduction in uncertainty) on global GPP estimates (Parazoo et al., 2014). Several attempts were made in this direction with various products derived from different satellite instruments or different processing chains. In this context, it is thus crucial to first compare and evaluate the information content brought by the different SIF products.

We have compared different SIF products to evaluate the most robust features that should be valorized. We are currently extending the initial study of Bacour et al. (2019) that compares three products from satellite measurements (one from OCO-2 and two from GOME2), including more recent products from TROPOMI instrument. Let us first recall the main points of the initial comparison done in Bacour et al. (2019). From the three products, they have selected an ensemble of grid points that would be representative of typical Plant

Functional Types of a land surface model. For each PFT they performed a cluster analysis in order to account for the diversity within each PFT in terms of climate, physiological, and structural characteristics, which would induce different SIF responses. The principle of the clustering approach is to minimize the variance within each cluster while maximizing the variance between clusters. Figure 7 illustrate the first two clusters of each PFT (when at least two clusters were identified). The main messages are:

- Potential bias may occur between different products.
- Two different processing chains applied on GOME-2 data can potentially lead to larger differences than those obtained from a different instrument.
- The most robust feature across SIF products is provided by phase of the seasonal cycle, while the amplitude of the seasonal cycle differs more substantially.

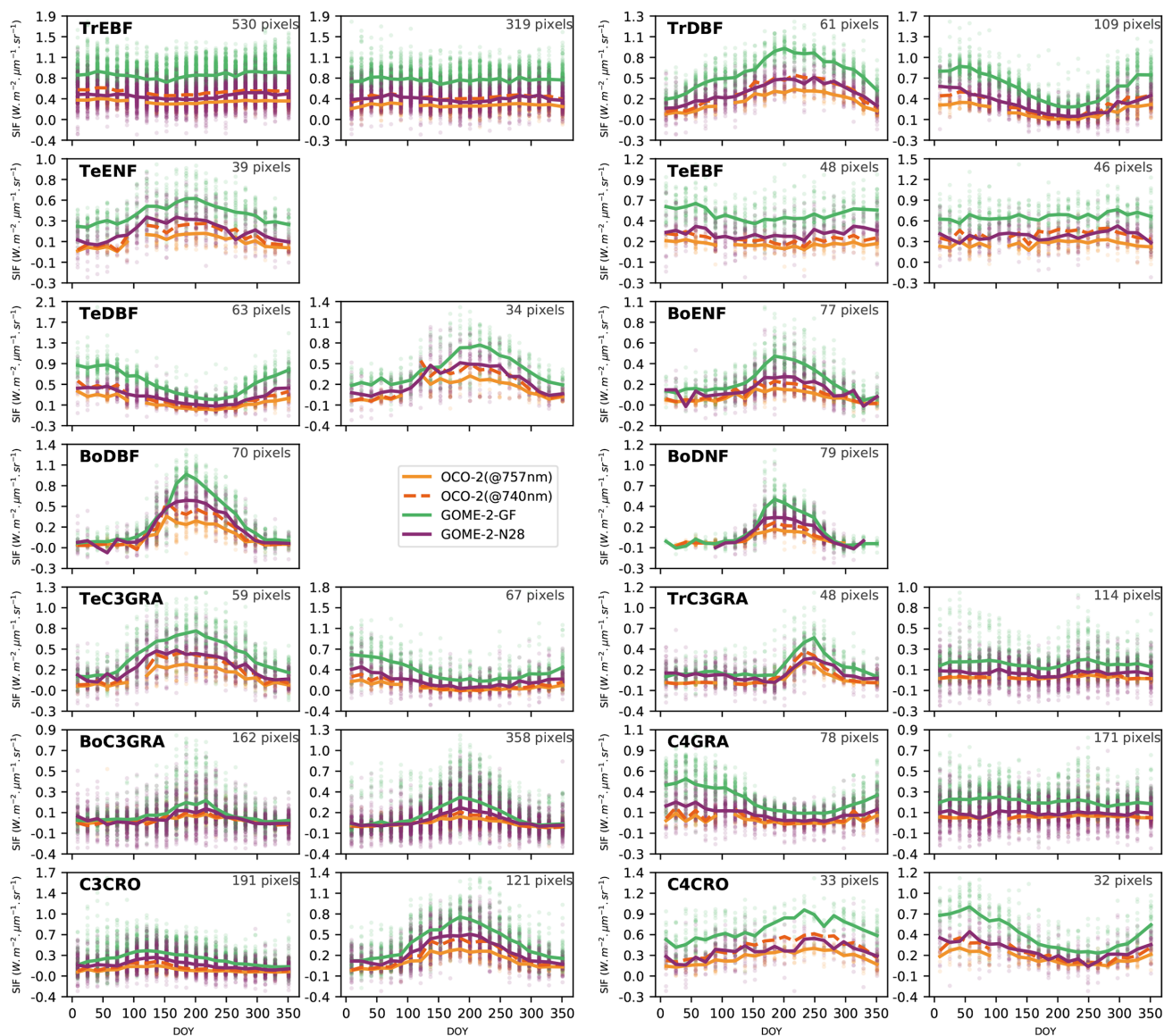


Figure 7: Examples of temporal variations of the SIF products for two clusters of each plant functional type (year 2015). The lines correspond to the means of the corresponding cluster and the dots to the actual products, with a different colour for each product. For OCO-2, the time series are shown for the raw (@757 nm) and spectrally scaled (@740 nm) data. The number of pixels considered in each cluster is indicated. The PFTs are tropical evergreen broadleaf (TrEBF), tropical deciduous broadleaf (TrDBF), temperate evergreen needleleaf (TeENF), temperate evergreen broadleaf (TeEBF), temperate deciduous broadleaf (TeDBF), boreal evergreen needleleaf (BoENF), boreal deciduous broadleaf (BoDBF), boreal deciduous needleleaf (BoDNF), forests, C3 grasslands (temperate—TeC3GRA, tropical—TroC3GRA, and boreal—BoC3GRA) and C4 grasslands (C4GRA), and C3 (C3CRO) and C4 (C4CRO) crops.

Compared to the previous missions, the TROPOspheric Monitoring Instrument (TROPOMI) onboard Sentinel-5 Precursor which combines a global continuous spatial sampling with a 5.5 km x 3.5 km pixel size at nadir, a daily revisit time, a wide spectral coverage, leads to an enormous improvement in the number of clear-sky measurements per day. We use the product derived by Caltech (Köhler et al. 2018) and the one derived in the frame of an ESA funded study for which we are involved. The retrieval scheme is mostly similar to that of Caltech but it uses a different cloud fraction product (derived from VIIRS for Caltech and from TROPOMI for our product). These products are first evaluated over vegetation free areas in order to quantify their bias. Over vegetated surfaces, they are evaluated in terms of mean seasonal cycle per ecosystems (phase and amplitude) but also in terms of spatial and temporal dynamic at high resolution in order to identify robust patterns of drought impacts on ecosystem fluxes. The selected data sets and the most robust spatial-temporal characteristics will be used in order to evaluate model GPP.

3.3 Observation-based water fluxes to constrain land carbon fluxes

Multiple novel observations-based datasets of water fluxes over land are available to help constrain carbon fluxes. Padrón et al. (2020) combine published datasets of global gridded runoff (R) (Ghiggi et al., 2019) and terrestrial water storage fluctuations (ΔTWS) (Humphrey and Gudmundsson, 2019) from 1902 to 2014 to obtain water availability estimates according to the water balance $P - ET = R + \Delta TWS$; where P is precipitation and ET is evapotranspiration. The datasets for both R and ΔTWS are reconstructions from statistical data-driven models (DDM) calibrated with observations, which perform well compared with state-of-the-art hydrological models (Ghiggi et al., 2019; Humphrey and Gudmundsson, 2019). Near-surface air temperature and P data are used as explanatory variables for both reconstructions. In addition, there are also estimates of all water cycle components from multiple land-surface model (LSM) simulations that are driven with observational atmospheric data (van den Hurk et al., 2016), which are available at <https://esgf-node.llnl.gov/search/cmip6/> under the experiment ID “land-hist”. A manuscript about the land water and carbon balances in these offline CMIP6 simulations is under preparation. The core atmospheric forcing data used for both the DDM and LSM reconstructions are from the Global Soil Wetness Project Phase 3 (GSWP3) (Kim et al., 2017). Although these reconstructions are not exempt from caveats such as not accounting for land-use changes (DDM), local land–atmosphere feedbacks (LSM) and groundwater withdrawal (DDM and LSM), they are complementary. Using both the DDM and LSM reconstructions, Padrón et al. (2020) identified an attributable contribution of human-induced climate change to the pattern of changes in dry season water availability around the world (Figure 8). Multiple regions have experienced increased drying in the dry season, particularly at extratropical latitudes. This result, together with the importance of low soil moisture as a stress on ecosystem production globally (Liu et al., 2020), highlight the relevance of observations-based land water fluxes to study the land carbon balance.

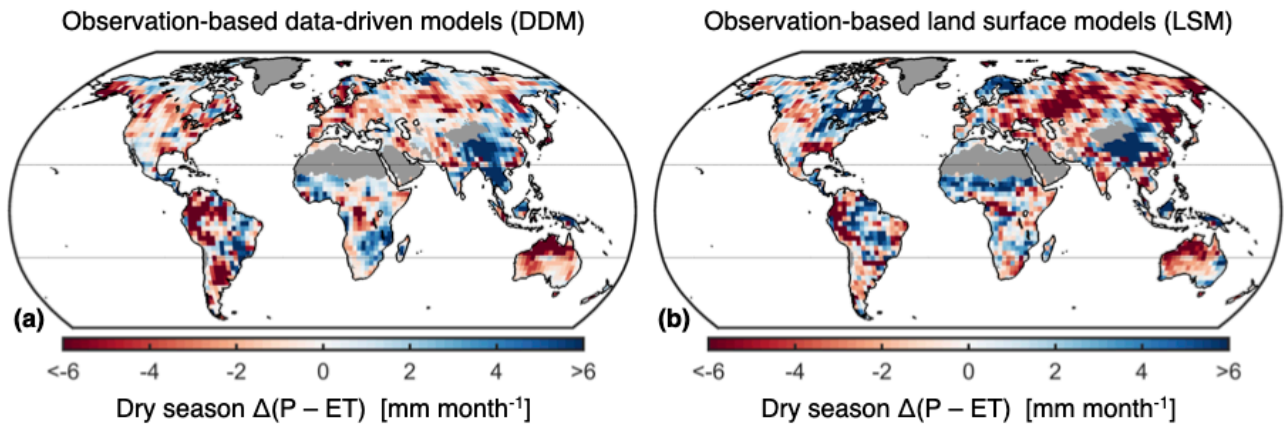


Figure8: Change in dry season water availability from the recent period 1985–2014 relative to the period 1902–1950 based on the reconstructions from (a) data-driven models (DDM) and (b) land surface models (LSM).

Further progress has been made by extending the runoff reconstruction from Ghiggi et al. (2019) to quantify the uncertainty in global runoff reconstructions that is implied by uncertainty in the atmospheric forcing data. To this end a multi-forcing observation-based global runoff reanalysis was developed (Ghiggi et al. in review). This comprehensive product is based on 21 different atmospheric forcing data sets (Figure 9) and provides uncertainty estimates by means of up to 525 stochastically generated ensemble members. The ensemble reconstruction is evaluated using independent observations that were not used for model calibration and compares favorably to global hydrological model simulations. This newly developed data product allows for new insights into the uncertainties of global water balance estimates, that are of relevance for carbon cycle research.

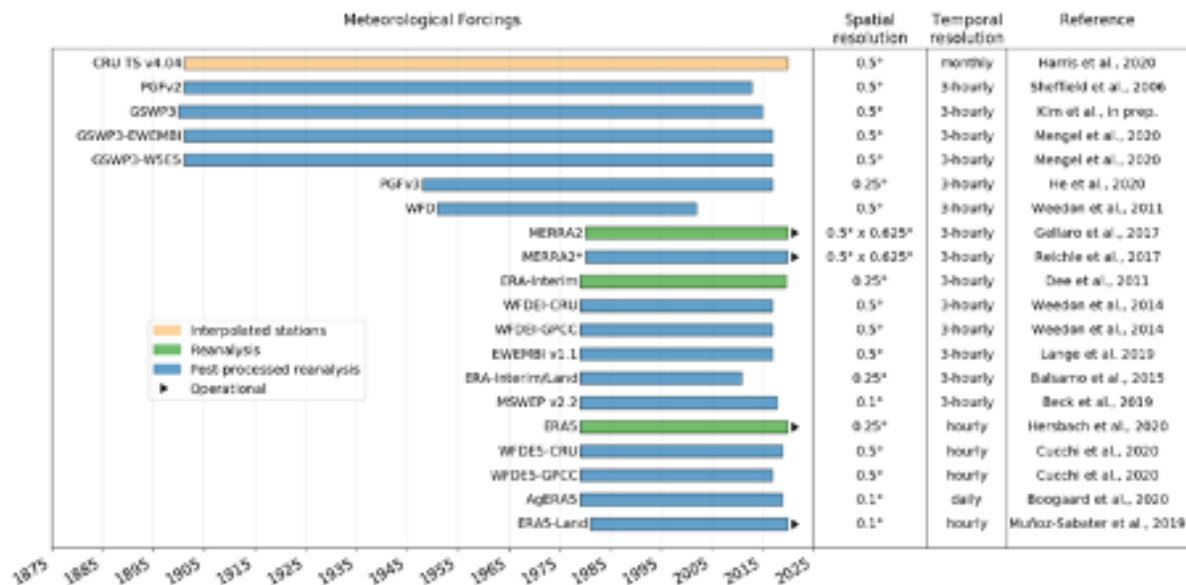


Figure 9: Atmospheric data sets contributing to the ensemble reconstruction of global runoff (Ghiggi et al, in review).

4 Publications from this deliverable

- Ghiggi, G., Humphrey, V., Seneviratne, S. I. and Gudmundsson, L. G-RUN ENSEMBLE: A multi-forcing observation-based global runoff reanalysis. *Water Resources Research*, in review, 2021.
- Liu, L., Gudmundsson, L., Hauser, M., Qin, D., Li, S. and Seneviratne, S. I.: Soil moisture dominates dryness stress on ecosystem production globally, *Nat. Commun.*, 11(1), 4892, doi:10.1038/s41467-020-18631-1, 2020.
- Padrón, R. S., Gudmundsson, L., Decharme, B., Ducharne, A., Lawrence, D. M., Mao, J., Peano, D., Krinner, G., Kim, H. and Seneviratne, S. I.: Observed changes in dry-season water availability attributed to human-induced climate change, *Nat. Geosci.*, 13(7), 477–481, doi:10.1038/s41561-020-0594-1, 2020.
- Maignan, F., Abadie, C., Remaud, M., Kooijmans, L. M., Kohonen, K. M., Commane, R., ... & Peylin, P. (2021). Carbonyl Sulfide: Comparing a Mechanistic Representation of the Vegetation Uptake in a Land Surface Model and the Leaf Relative Uptake Approach. *Biogeosciences Discussions*, 1-41.

5 Additional references

- Bacour, C., Maignan, F., Peylin, P., MacBean, N., Bastrikov, V., Joiner, J., ... & Frankenberg, C. (2019). Differences between OCO-2 and GOME-2 SIF products from a model-data fusion perspective. *Journal of Geophysical Research: Biogeosciences*, 124(10), 3143-3157.
- Ghiggi, G., Humphrey, V., Seneviratne, S. I. and Gudmundsson, L.: GRUN: an observation-based global gridded runoff dataset from 1902 to 2014, *Earth Syst. Sci. Data*, 11(4), 1655–1674, doi:10.5194/essd-11-1655-2019, 2019.
- Humphrey, V. and Gudmundsson, L.: GRACE-REC: a reconstruction of climate-driven water storage changes over the last century, *Earth Syst. Sci. Data*, 11(3), 1153–1170, doi:10.5194/essd-11-1153-2019, 2019.
- Kim, H. J.: Global Soil Wetness Project Phase 3 Atmospheric Boundary Conditions (Experiment 1), *Data Integr. Anal. Syst.* [online] Available from: <https://doi.org/10.20783/DIAS.501>, 2017.

- Köhler, P., Frankenberg, C., Magney, T. S., Guanter, L., Joiner, J., & Landgraf, J. (2018). Global retrievals of solar-induced chlorophyll fluorescence with TROPOMI: First results and intersensor comparison to OCO-2. *Geophysical Research Letters*, 45(19), 10-456.
- Launois, T., P. Peylin, S. Belviso & B. Poulter. A new model for the global biogeochemical cycle of carbonyl sulfide – Part 2: Use of carbonyl sulfide to constrain gross primary productivity in current vegetation models. *Atmos. Chem. Phys.* 15: 9285–9312, 2015.
- Montzka, S, & Tans, P. 2004. Can Carbonyl Sulfide Help Constrain Gross Vegetative Fluxes of Carbon Dioxide? In: AGU Fall Meeting Abstracts.
- Sandoval-Soto, L, Stanimirov, M, Von Hobe, M, Schmitt, Vivien, Valdes, J, Wild, A, & Kesselmeier, J. 2005. Global uptake of carbonyl sulfide (COS) by terrestrial vegetation: Estimates corrected by deposition velocities normalized to the uptake of carbon dioxide (CO₂). *Biogeosciences*, 2 (2), 125–132.
- Seibt, U, Kesselmeier, J, Sandoval-Soto, L, Kuhn, U, & Berry, JA. 2010. A kinetic analysis of leaf uptake of COS and its relation to transpiration, photosynthesis and carbon isotope fractionation. *Biogeosciences*, 7 (1), 333–341.
- van den Hurk, B., Kim, H., Krinner, G., Seneviratne, S. I., Derksen, C., Oki, T., Douville, H., Colin, J., Ducharne, A., Cheruy, F., Viovy, N., Puma, M. J., Wada, Y., Li, W., Jia, B., Alessandri, A., Lawrence, D. M., Weedon, G. P., Ellis, R., Hagemann, S., Mao, J., Flanner, M. G., Zampieri, M., Materia, S., Law, R. M. and Sheffield, J.: LS3MIP (v1.0) contribution to CMIP6: the Land Surface, Snow and Soil moisture Model Intercomparison Project – aims, setup and expected outcome, *Geosci. Model Dev.*, 9(8), 2809–2832, doi:10.5194/gmd-9-2809-2016, 2016.
- Whelan, Mary E., et al. "Reviews and syntheses: Carbonyl sulfide as a multi-scale tracer for carbon and water cycles." *Biogeosciences* 15.12 (2018): 3625-3657.